REVIEW

Tackling SNR at low-field: a review of hardware approaches for point-of-care systems

Andrew Webb[1] · Thomas O'Reilly[1]

Abstract

Objective To review the major hardware components of low-field point-of-care MRI systems which affect the overall sensitivity.

Methods Designs for the following components are reviewed and analyzed: magnet, RF coils, transmit/receive switches, preamplifiers, data acquisition system, and methods for grounding and mitigating electromagnetic interference.

Results High homogeneity magnets can be produced in a variety of different designs including C- and H-shaped as well as Halbach arrays. Using Litz wire for RF coil designs enables unloaded Q values of ~ 400 to be reached, with body loss representing about 35% of the total system resistance. There are a number of different schemes to tackle issues arising from the low coil bandwidth with respect to the imaging bandwidth. Finally, the effects of good RF shielding, proper electrical grounding, and effective electromagnetic interference reduction can lead to substantial increases in image signal-to-noise ratio.

Discussion There are many different magnet and RF coil designs in the literature, and to enable meaningful comparisons and optimizations to be performed it would be very helpful to determine a standardized set of sensitivity measures, irrespective of design.

Keywords Low-field MRI · Magnets · RF coils · Point-of-care · Grounding · Shielding · Litz wire

Introduction

The recent growing interest in mid-field (0.1–1 T), low-field (0.01–0.1 T) and point-of-care (POC) MRI has been driven by the concept of increasing the accessibility of a traditionally extremely expensive imaging modality. The increased accessibility of mid-field systems can be related primarily to reduced purchase, maintenance and infrastructural costs, and increased availability for patients with contraindications such as medical implants, compared to conventional (1.5–3 T) field strengths. POC low-field systems, which are designed to be portable, increasing access to MRI by enabling it to be used in situations in which it has not previously been possible: examples include the intensive care unit, emergency rooms and ambulances in the developed world, and sites in lower and middle income countries (LMICs) which lack the finance and/or infrastructure for conventional MRI systems.

The major technical challenge of mid-field and low-field MRI in general is, as expected, that of signal-to-noise ratio (SNR). For POC systems, the limited B_0 field homogeneity is a challenge, arguably equal to that of low SNR. This is primarily due to the reduced size of such systems, which means that the imaging field-of-view lies very close to the inner surface of the magnet. From a hardware point-of-view, the major contributing components to SNR are the magnet, in terms of both strength and homogeneity, the RF coil(s) in terms of sensitivity, and the receiver chain in terms of total noise figure. Each of these is considered in this review article.

Starting from well-known equations, the magnetization (M_0) per unit volume of tissue can be expressed as:

$$M_0 = \frac{N\gamma^2 h^2 I(I+1)B_0}{12\pi^2 k_B T_s} \tag{1}$$

where N is the number of spins per unit volume, γ is the gyromagnetic ratio, h is Plank's constant, I is the spin

✉ Andrew Webb
a.webb@lumc.nl

1 Department of Radiology, C.J. Gorter MRI Center, Leiden University Medical Center, 2333 ZA Leiden, The Netherlands

angular momentum, B_0 the main magnetic field, k_B Boltzmann's constant, and T_s the sample temperature, which is assumed to be body temperature. The magnitude of the MR signal (S) in the rotating frame (ignoring relaxation) is given by:

$$S = \frac{K\omega_0 B_1^- M_0 V_s}{i} \quad (2)$$

where i is the current in the coil, and assuming that a single coil is used for transmit and receive the conventional B_1^+/i term can be replaced by B_1^-/i, K is a numerical factor (between 0 and 1) which essentially is a measure of the integrated sensitivity of the coil compared to that if the B_1 field were perfectly uniform, V_s is the volume of the sample, and ω_0 is the resonance frequency.

The noise (from both the RF coil and the sample) is given by:

$$N_s = \sqrt{4k_B T R \Delta f} \quad (3)$$

where N_s is the root mean square noise voltage, R the total system resistance and Δf the measurement bandwidth. There are two components to the total resistance, body (sample) loss and RF coil loss, which can be represented as respective resistances, R_{body} and R_{coil}: the total resistance is simply the summation of these two quantities. Body loss can be further subdivided into magnetic losses due to B_1-induced currents in the body and electric losses due to capacitive coupling between the coil and the body [1–6]. In general, it is assumed that if the RF coils are properly constructed, then the body loss is dominant at clinical field strengths, unless very small receiver coils are used. For low-field systems, coil noise represents a substantial component of the total system noise [5–7].

In terms of mid-field MRI, there have been many reports recently associated with systems operating at 0.55 T [8–19]. Somewhat naively, one might expect the SNR to be approximately one-quarter that at 1.5 T. However, a number of factors work to the advantage of the lower field, and reduce the loss factor. Tissue T_1 relaxation times are shorter at 0.55 T, with the T_2 values being roughly equal, and the T_2^* time longer, particularly in tissues where there is a strong contribution from tissue micro-inhomogeneities or strong dephasing due to the presence of iron (e.g., liver) or air (e.g., the lungs). For bSSFP sequences the signal intensity is proportional to T_2/T_1, and so are more SNR efficient at lower fields. In addition, the acquisition bandwidth can be reduced by a factor-of-three compared to that at 1.5 T (assuming that one maintains the water/fat shift constant in terms of the number of pixels), reducing the Johnson noise. Marques et al. [20] provided a theoretical analysis of the optimization of sequence parameters as a function of field strength, and concluded that the B_0

dependence was approximately linear, rather than a 3/2 power relationship. Campbell-Washington et al. have provided experimental demonstrations at 0.55 T that the use of highly efficient sequences such as long spiral readouts, or turbo spin echo with full 180° refocusing pulses or balanced steady state free precession sequences with higher tip angles than used at 1.5 T [8–19], can increase the SNR at lower fields, with the extreme case of lung imaging actually giving higher SNR at 0.55 T than at 1.5 T. For most tissues, it has been estimated [21] that the SNR at 0.55 T is approximately 70% that at 1.5 T. The same form of analysis can be performed even for whole-body ultra low field systems (< 0.01 T), e.g., the work initially presented at 6.5 mT by Sarracanie et al. [22], based on a previous electromagnet [23, 24], and follow-up publications [25–27], in which the very homogeneous B_0 field enabled efficient balanced SSFP sequences to be run, with an impressive resulting SNR given the very low B_0 field.

For small, portable POC systems based on permanent magnets, there are many more design parameters that need to be considered to optimize SNR, and there are strong interdependencies between these parameters. In this regard, the critical differences between a POC and conventional MRI system include that for a POC system the B_0 field is much more inhomogeneous, the gradient strengths are much weaker, the available space is much less and so the physical distance between RF coil, RF shield and gradient coils is very small. Some of the issues mentioned in the discussion of the 0.55 T system are also relevant, in particular the lower T_1 tissue value, which increases the available SNR per unit time. However, unlike for a whole-body 0.55 T system, in general the acquisition bandwidth cannot be significantly decreased compared to a clinical scanner due to the relatively inhomogeneous B_0 and the limited gradient strength, otherwise significant point-spread-function (PSF) broadening/imaging distortions would occur in the frequency encoding process (phase encoding is essentially immune to this effect). The inhomogeneous B_0 also means that balanced SSFP, echo planar imaging (EPI) and spiral readouts are challenging to implement.

An example of the design trade-offs is that increasing the diameter of the magnet has the disadvantage of reducing the B_0 field, but the advantage of the larger bore allowing the RF shield to be located further away from the RF coil, increasing the coil sensivity. For this larger diameter magnet, the gradient coil diameter can also be increased which reduces the gradient efficiency but increases the usable imaging volume. A larger magnet also reduces the B_0 inhomogeneity over a given field-of-view and so the acquisition bandwidth can be decreased. As a result of some of these design trade-offs, there are a wide variety of designs and design philosophies of magnet, gradient coils, and RF coils for POC systems [22, 28–37]. The final SNR is, therefore, a complicated function

of all of these parameters, which constitute the main body of this review article.

System design for POC systems

(i) Magnet

There are two basic designs currently used for POC low field MRI systems: C- and H-shaped yoked magnets, and Halbach-based arrays. There are relative advantages and disadvantages of each of the designs. A C- or H-based system is much easier to construct. In addition, it is a more open structure. However, the Halbach system is much safer to construct due to the magnetic forces being divided over thousands of small magnets. Gradient coils for the parallel plates are planar, which are intrinsically less efficient than the cylindrical ones which used in a Halbach array. Radiofrequency (RF) coil design is similar, although coupling to the gradient coils is higher in the Halbach design. As outlined previously, the key elements in terms of sensitivity are the B_0 field strength and the homogeneity.

The basic design for C- and H-shaped magnets are two pole pieces of magnetic material such as neodynium boron iron or samarium cobalt, each disc shaped and of equal strength and situated above and below the imaging field of view. Normally, each disc is identical in construction, with the material polarized in the vertical direction. The discs are placed with the same polarity in the vertical direction so that the magnetic field add together in the imaging volume. The two discs are connected by a ferromagnetic yoke (usual made of steel), which is not magnetically saturated, but which increases the magnetic field strength between the two discs. There is an optimum spacing between the discs, in relation to the radius of each disc, which maximizes the B0 field homogeneity [38, 39]. To further improve the homogeneity, smaller permanent magnets can be placed in suitable locations and/or electrical systems for shimming incorporatedfor low-field MRI applications [34, 35, 40, 41].

Enhancing the magnetic field on one side of a magnet array while cancelling the field on the other side was first demonstrated by Mallinson [42]. Halbach [43, 44] laid down a set of rotation rules which gave rise to different multipole field modes inside a cylindrical magnet array: the magnetization along the periphery of the circular cross-section at an azimuthal angle θ should be arranged at an angle $\alpha = (N+1)\theta$, where N defines the mode. For $N = 1$, there is a 2θ variation which produces a dipole field structure, $N = 2$ gives a quadrupole field and so on. The Halbach configuration has been shown to produce the strongest possible field per unit mass of magnetic material [45, 46]. The rotation rules given by Halbach work best for infinitely long cylindrical arrays with a circular

cross-section: in the dipole configuration one obtains a perfectly homogeneous field distribution at the centre of the array. However, practical Halbach cylindrical magnets of finite length suffer from significantly lower field homogeneity. Much research has concentrated on improving the field homogeneity of a finite-length circular cross-section magnet array consisting of a large number of discrete magnet elements. Parameters which have been optimized include the rotation angle of individual magnets, spacing between separate rings of magnets, and the strength and orientation of the magnets themselves [29, 47–58].

The magnetic flux density (B) in an ideal Halbach dipole array is given by:

$$B = B_R \ln \frac{r_o}{r_i} \tag{4}$$

where B_R is the remanence of the magnetic material, and r_o and r_i the outer and inner radii of the annular magnet. In addition, since continuous pieces of magnetic material with spatially varying magnetization cannot be produced in practice, the arrays consist of a number of discrete individual magnet elements (these were termed NMR-Mandhalas, but for consistency with existing literature we use the term Halbach to include the discrete Mandhala designs). These structures generate a smaller field than would originate from a continuous magnetic material, because the space between r_o and r_i is not completely filled with magnetic material. There is a reduction of about 50% in B_0 for magnets with a square cross-section, and ~25% flux reduction magnets with octagonal or circular cross-section. Overall, discrete Mandhalas and continuous Halbachs produce almost identical B_0 field per unit mass of magnetic material. In terms of B_0 homogeneity, discretization using polygonal magnets increases the inhomogeneity by ~20–30% compared to a continuous Halbach, with the square/cubic magnets producing up to an order of magnitude poorer homogeneity. Blumler [44, 45] also reported that these values depend on the number of magnets used in the discretization, and almost exponentially on the radius of the volume over which the homogeneity is determined. Figure 1 shows schematics of a discrete Halbach magnet, as well as an illustration of the dependence of the B_0-homogeneity on the length:diameter ratio.

Whether the designed system is C-/H-shaped or a Halbach array, it requires substantial B_0 shimming to reach its theoretical optimal homogeneity. This is primarily due to small errors in exact magnet positioning, and small non-uniformities in the properties of the magnetic materials. The major challenge is that, since the imaging field-of-view is a substantial fraction of the total magnet volume, the inhomogeneities are large compared to conventional clinical MR magnets, and also contain higher order terms close to the magnet surfaces. B_0 shimming

20 cm diameter, 20 cm length
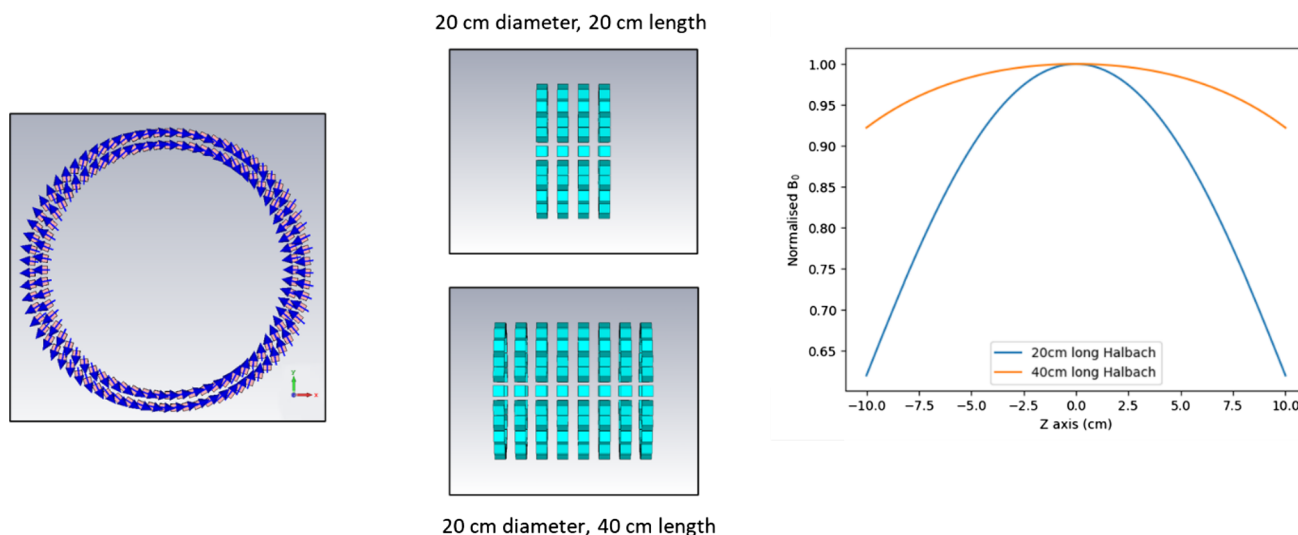

20 cm diameter, 40 cm length

Fig. 1 Schematics of a Halbach array constructed from a large number of individual magnets. (left) Front view of the orientation of the individual magnet dipoles (north/south). Centre and right show that a larger length:diameter ratio produces a more homogeneous B_0 field (the line is plotted along the centre of the magnet in the front-to-back direction)

can be performed using small permanent magnets (fixed shimming) or by passing current through extra conductive shim coils (case-by-case shimming), as well as a combination of both approaches. Typically, B_0 homogeneity is measured using a three-axis Hall probe with some form of robotic positioning device. Uberruck et al. [59] investigated two different approaches for using permanent magnets to shim C- and H-shaped magnets for a table-top system, one which used a hexagonal array of 37 small magnets in a hexagonal arrangement, and the other which used four rings of permanent magnets which could be physically displaced. Lopez et al. [60] presented a passive shim design method based on expressing the shim distribution as a sum of orthogonal functions, and solving for the coefficients to determine the positioning of sets of permanent magnets. McDowell and Conradi [61] designed a set of very thin wire higher order electrical shim coils for a small tabletop system based on a dipolar magnet. Terada et al. [40] used a combination of permanent magnets and a single electrical shim coil for a compact 0.3 T system for imaging the human hand. For Halbach arrays, Parker et al. [62] described a system based on a core unit of two nested Mandhalas comprising hexagonal magnets, and a shim unit consisting of identical hexagonal magnets in outer shells. Wenzel et al. [63] used an iterative scheme and genetic algorithm to design as set of shim magnets for a small Halbach magnet with an imaging field-of-view of 4 cm. Wang et al. [64] proposed a shimming method based on sheets of permanent magnet material targeting at spherical harmonic basis up to the 3rd order including dedicated composition of $Y(4Z^2-X^2-Y^2)$, Z^3 and

$X(4Z^2-X^2-Y^2)$ ($n=3$, $m=-1, 0, 1$) with cross terms to implement structural field compensation.

(b) *RF coils*

The basic aim of RF coil design, in terms of maximizing SNR, is to ensure that the coil loss represents as small a fraction of the body loss as possible. This is not difficult at the frequencies used for conventional clinical MRI, but becomes more challenging at low frequencies, and indeed is not attainable at frequencies in the tens to hundreds of kHz range [65].

(a) *Geometry*

RF coil designs can be both transmit and receive (Tx/Rx), or have separate coils for transmit (Tx) and receive (Rx), which must obviously be isolated from one another, using either geometrically orthogonal designs or switchable detuning circuits. The transverse orientation of the B_0 field in most POC systems (C-shaped, H-shaped and Halbach, although not O-shaped [37]), allows the use of a solenoidal geometry for the RF coil. Variations of the solenoid, which more closely conform to the geometry of the head, are also commonly used. As shown many years ago, the solenoid is between a factor-of-two and three more sensitive (B_1/I) [66] than a linear saddle or birdcage coil (of course a quadrature birdcage or saddle coil cannot be used in this configuration), with a slightly poorer B_1 homogeneity measured over the active region of the coil. If separate Tx and Rx coils are used, then a solenoid is used as the receive element

and either a second solenoid (the two solenoids must each contain actively switchable detuning circuits) or an intrinsically-geometrically-decoupled saddle coil can be used as the transmit element.

It is worth noting that some systems, both academic [67–69] and also the Hyperfine Swoop, have incorporated arrays of receive elements, similar to the situation for clinical MRIs. These receive elements are loop coils with various geometries and sizes. To date, no comparison has been made between the SNR of these arrays compared to a single receiver, and there is little information on parallel imaging performance. Although the geometry (g-factors are likely to be relatively large given the low influence of the sample on coil isolation), there may be cases where the SNR is sufficiently high such that meaningful reductions in total scan time can be achieved without losing significant diagnostic utility.

(b) *Conductor dimensions*

As covered in many publications [70], general fabrication rules for RF coils include the recommendation that the total length of the conductor should be less than $\lambda/20$ such that substantial wavelength effects are not present. Capacitive segmentation is standardly used in high frequency RF coils as a method to reduce dielectric losses in the body, phase shifts along the length of the coil conductor, and SAR arising from conservative electric fields around individual capacitors in the impedance matching network. The use of capacitive segmentation has been discussed much less for low field coils, but nevertheless is worth incorporating. For example, the wavelength at 2 MHz is ~150 m in a copper conductor, although the effective wavelength may be shorter in helices due to compression effects (inter-turn capacitance between turns). This corresponds to a $\lambda/20$ of 7.5 m, which for a circular solenoid of diameter of 27 cm, represents only ~9 turns.

In terms of how large the diameter of the conductor should be, and how close the turns should be, there are two effects which need to be considered, shown schematically in Fig. 2.

The resistance of a solenoidal coil, corresponding to Johnson noise, is given by [2]:

$$R_{\text{coil}} \cong \frac{3\zeta n^2 a}{l\sigma\delta} \tag{5}$$

where ζ is the proximity effect factor (see below), σ is the conductivity of the conductor, n is the number of turns, a is the coil radius and l the coil length, and δ is the frequency-dependent skin-depth, in turn given by:

$$\delta = \sqrt{\frac{\rho}{\pi f \mu_0}} \tag{6}$$

where ρ is the resistivity, f the frequency, and μ_0 the magnetic permeability. The effective cross-sectional area, A_{eff}, which carries current is given by:

$$A_{\text{eff}} = \pi d_0 \sqrt{\frac{\rho}{\pi f \mu_0}} \tag{7}$$

The DC resistance of a wire conductor is inversely proportional to the square of the wire diameter, whereas the skin effect is linearly proportional to the diameter, so overall the ratio $R_{\text{AC}}/R_{\text{DC}}$ decreases inversely with wire diameter. The skin depth at 2 MHz in copper is ~47 μm, meaning that 95% of the current is within the outer 0.15 mm. So for example, the AC resistance is ~10 times the DC resistance for a 2 mm diameter copper wire.

If two wires carrying AC current in the same direction (i.e., parallel wires) are brought into close proximity then the spatial distribution of the currents within each wire changes. The magnetic field of the first wire induces eddy currents in the second wire, that form loops along the wire. These
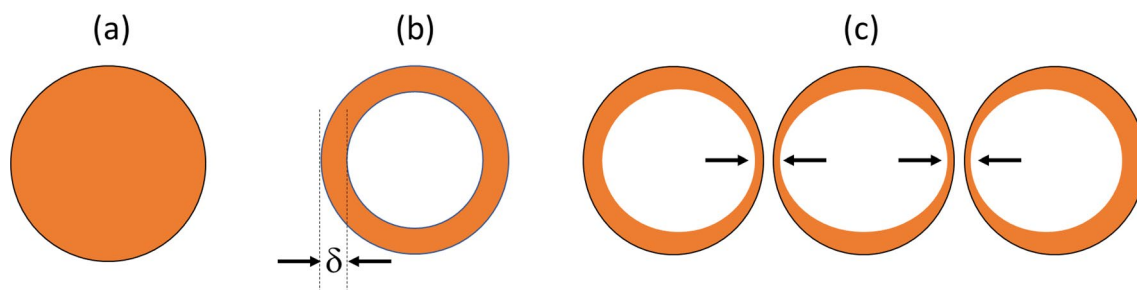

Fig. 2 Schematic of the current distribution in a circular cross-section conductor. **a** At zero-frequency direct current (DC) the current is distributed uniformly throughout the wire. **b** Illustration of the skin effect for an AC current, in which the current is maximum at the outside of the conductor, and falls off exponentially with depth with the exponent given by the skin depth (δ). The decrease in effective cross-sectional area means that the AC resistance is higher than the DC resistance. **c** Illustration of the proximity effect (shown by the arrows) for a number of parallel conductors. This reduces even further the cross-sectional area through which the current flows, increasing its resistance

eddy currents flow in the same direction as the current on the side of the second wire facing away from the first wire, and back in the opposite direction on the side of the second wire facing the first wire. In other words, the overall effect is to redistribute the current in the second wire into a thin cross-sectional area on the side furthest away from the first wire. Since the current is concentrated into a smaller area of the wire, the resistance is increased: this is known as the proximity effect. This effect is shown in Fig. 1c. If the wires in the RF coil are wound very close together then the proximity factor can be very large, up to a factor of 10 if large conductors are used. However, if a separation between the wire centres of twice the wire diameter is used, then the proximity effect drops to ~ 10–15% [66].

Based on these results, the optimum wire diameter for a solenoid would be several cm (see for example, Fig. 4.7 in Chen and Hoult [70]). However, given space restrictions within a typical POC system this diameter is simply not practical, and so rather than use suboptimal thin single conductors, the solution is to use Litz wire. This consists of many thousands of very thin insulated strands of wire, each one which has a diameter smaller than the skin depth, which are braided around each other to ensure that equal current flows in each strand. For Litz wire, containing N_s strands with diameter d_{litz}, if $d_{litz} << \delta$, then the proximity effect can be estimate from:

$$A_{eff} = N_s \frac{\pi d_{litz} \delta}{4} \tag{8}$$

Hoult showed that the Q-factor is optimized using a wire separation of approximately 1.5 times the wire radius [66], but for Litz wires the turns can be placed very close together without any proximity effects. For frequencies between 1.4 and 2.8 MHz a wire diameter of ~ 30 microns is optimal. Litz wire has shown to be a feasible approach for constructing RF coils up to 10 MHz [71].

One of the most detailed studies involving Litz wire was by Resmer et al. [72] who derived parameters for optimizing the Q-factor and SNR for a multi-turn surface coil at 0.01 T. For solid wire, at low frequencies (< 1 MHz) the skin-effect is much more pronounced than the proximity effect, and so Q values increase as the square root of the frequency. As the frequency approaches the self-resonance frequency of the coil, then dielectric losses arising from the self-capacitance begin to play a larger role, and these increase as the third power of frequency. For Litz wire, at low frequencies DC losses are greater than the skin depth and so the Q value increases linearly with frequency. At higher frequencies the proximity effects become higher, and beyond its maximum value the Q is proportional to $1/f$. Including dielectric losses reduces the maximum Q value, and also shifts it to lower frequencies.

In addition to coil losses there are three other loss mechanisms: inductive and dielectric losses which are both associated with the sample, and radiation losses. From Maxwell's equations, the alternating B_1^+ field induces magnetically induced (inductive) losses, also known as eddy current losses, in a conducting sample. These losses can be represented as an effective resistance R_m in series with the receiving coil, using a model originally suggested by Gadian and Robinson [5]. The value of R_m is proportional to the square of the operating frequency and the sample conductivity. Dielectric losses result from electrical lines of force, associated with the distributed capacitance of the RF coil, passing through the sample. Gadian and Robinson [5] showed that these dielectric losses could be modelled as a parallel stray capacitance between the coil and the sample, with the conducting sample represented as a parallel resistor (R_e) and capacitor. At low frequencies R_e is proportional to the fourth power of frequency, in the high frequency limit to the square of the frequency. The higher the sample conductivity the higher the value of R_e and the higher the losses. R_e is also proportional to the square of the inductance of the coil. Radiation loss, which represents energy radiated away from the coil rather than into the sample. Radiation loss can be correlated to an equivalent resistance, $R_{radiation}$, which is proportional to the fourth power of both frequency and coil radius. Except for very large coils at very high frequencies, the coil resistance is much higher than the radiation resistance.

Experimentally one can measure the Q value as a function of frequency to determine the transition between coil noise dominance and body noise dominance [65]. Experimentally this is best performed using two pick up loops placed either side of the coil, and measuring the S_{21} scattering parameter [73]: the Q value can then be estimated as the full-width-half-maximum (FWHM) of the peak. By defining a loading factor (LF):

$$LF = 1 - \frac{Q_{loaded}}{Q_{unloaded}} \tag{9}$$

If the LF > 0.5 then coil noise dominates, and if LF > 0.5 coil noise dominates.

Figure 3 exemplifies the principles described in the previous sections. Three solenoidal RF coils were constructed, one with 1 mm diameter copper wire, one with 2 mm diameter copper wire, and one with Litz wire with 1500 strands of 30 μm diameter copper wire. The respective loaded and unloaded Q values of the coils were 88, 240 and 360. Each coil is impedance matched to 50 Ω using parallel tuning capacitors ~ 1 nF and series matching capacitors ~ 100 pF.

The SNR is theoretically proportional to the square root of the Q value. We performed experiments on a uniform gel-based phantom to test this using the three coils shown in

Fig. 3 Different solenoidal coils constructed from thin wire (left), thicker wire (centre) and Litz wire (right). The respective unloaded Q values are 88, 240 and 360

Fig. 3. The respective values were SNR 15.4 ($Q = 88$), 23.5 ($Q = 240$) and $Q = 31.2$ ($Q = 360$).

(c) *Effects of RF shielding*

As mentioned previously, the compact nature of head scanners means that the conductors of the RF coil are intrinsically very close to the inner Faraday shield. As the shield comes closer to the coil, the transmit field becomes increasingly located between the shield and the RF coil, and the B1 + magnitude in the sample is correspondingly lower. The effect can be analyzed in terms of "mirror currents", also known as "image currents", which correspond to counter-currents located outside the shield. The closer the shield to the RF coil, the greater the reduction in transmit efficiency, with a theoretical value of zero if the shield is coincident with the RF coil. This topic is extensively covered in pages 364–371 of Mispelter et al. [74]. An example is shown in Fig. 4, in which electromagnetic simulations were performed using an elliptical spiral coil with dimensions 180 mm width,
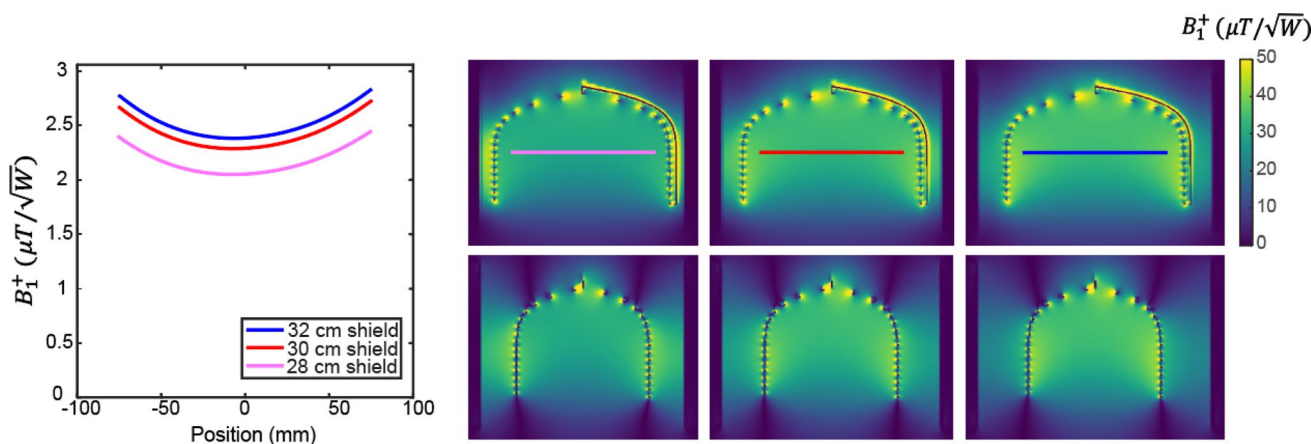

Fig. 4 Electromagnetic simulations of the transmit efficiency as a function of RF shield diameter for an elliptical spiral coil with dimensions $180 \times 240 \times 170$ mm. For smaller diameters the field becomes more concentrated between the coil and the shield. The line plots show an ~20% increase in transmit efficiency between the 28 and 32 cm diameter shield

240 mm height, and 170 mm length and different circular RF shields with diameters 280 mm, 300 mm and 320 mm. The results show that relative to a 280 mm shield, then there is a 15% increase in transmit (and therefore also receive sensitivity and SNR) if the shield diameter in increased to 300 mm and a ~ 20% increase for a 320 mm shield.

(iii) Receiver chain

The other major hardware component which affects the overall system sensitivity is the receiver chain, shown in Fig. 5. This consists of a transmit/receive switch (when a single Tx/Rx coil is used), preamplifier, second stage variable amplifier and the analogue-to-digital converter. Each component in the receive chain adds noise, and one can define the reduction in SNR in terms of a noise figure (NF) defined as:

$$NF(dB) = 20 \log \left(\frac{SNR_{in}}{SNR_{out}} \right) \tag{10}$$

The overall NF for the entire receive chain can be calculated from:

$$NF_{total} = NF_{Tx/Rx} + NF_{preamp} + \frac{NF_{amp}}{G_{preamp}} + \frac{NF_{ADC}}{G_{preamp}G_{amp}} \tag{11}$$

Unlike in much higher frequency MRI systems, the Tx/Rx switch and preamplifier can be placed a significant distance away from the RF coil with negligible cable loss. For example, cable losses in RG 58 at 2 MHz are approximately 1.5 dB per 100 m, with a capacitance of 100 pF per metre.

(a) Tx/Rx switch

Tx/Rx switches can either be passive or active: in either case the most common design is based on the impedance transformation properties of a quarter-wavelength cable, or lumped element equivalent as is much more practical at low-field. Crossed PIN-diode passive designs are essentially the same as those used at higher frequencies, with pi-networks using capacitors and inductors replacing the quarter-wavelength transformer, as shown in Fig. 6a. Active PIN-diode-based switches are also based on this prinicple. PIN-diode drivers and switches for the TRASE experiments at 8 MHz were described by Der et al. [75].
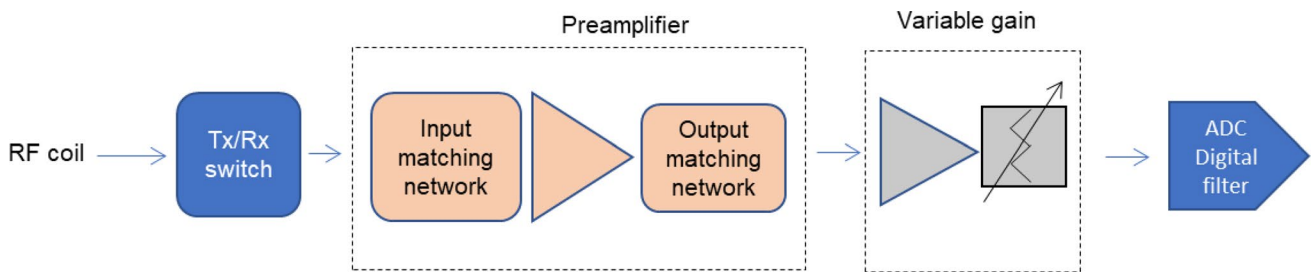

Fig. 5 Schematic of the receiver chain. For a receive-only coil the Tx/Rx switch may be omitted if isolation is sufficient
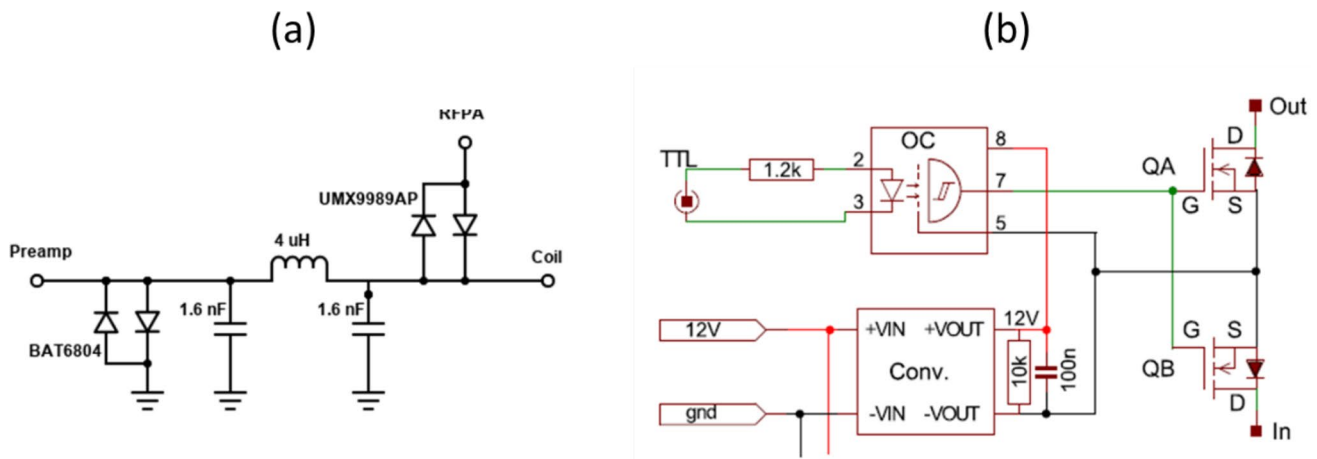

Fig. 6 Schematics of **a** a passive Tx/Rx switch designed for operation at ~ 2 MHz and **b** a fast MOSFET switch for operation at frequencies < 150 kHz [76]

PIN diodes do not work as well at very low frequencies since the RF filters or bias-T schemes used for PIN-diode bias control prevent switching times from being shorter than at least several RF periods. Nacher et al. [76] described the performance of a fast MOSFET-based switch, shown in Fig. 6b, designed for frequencies less than 150 kHz. High power switches using reed relays have been described by Straney et al. again for frequencies in the tens to hundreds of kHz range [26].

As can be seen from equation [11] the NF for the Tx/Rx switch is very important in the overall NF of the receiver chain. A typical loss, which is the same as the NF, for Tx/Rx switches is in the range of 0.2–0.3 dB.

(b) *Preamplifier*

In situations where the receive coil has a loaded Q value corresponding to a bandwidth which is much greater than the bandwidth used during image acquisition, then the coil is usually connected to a high gain (20–30 dB), low noise (0.5–1.2 dB) preamplifier with 50 Ω input and output impedance. The rationale at higher frequencies is that the connections between coil and preamplifier are usually via 50 Ω coaxial cable, and therefore to avoid reflections and power loss, all impedances are matched to 50 Ω. At frequencies in the low MHz range, such considerations are much less important: the preamplifier can easily be incorporated into the coil, or even if connected to the preamplifier via a 1 m long coaxial cable, the wavelength is several hundreds of metres and so losses are extremely small and reflections unimportant.

The preamplifier most commonly used in conventional MRI systems is based on a gallium arsenide field effect transistor (GaAs FET), but these are very difficult to obtain commercially at low frequencies, although there are designs in the literature with reported noise figures less than or close to 1 dB [77, 78]. At frequencies in the low MHz range then silicon germanium (SiGe) bipolar transistors are more available commercially, with noise figures ~ 1 dB (e.g., Wenteq Microwave, CA, USA). The input impedance of FETs and bipolar transistors is very high, several tens of kΩ up to MΩ. It is not possible to optimize both NF and gain at the same time. If Z_{in} is matched to 50 Ω this gives the maximum gain, but a higher noise figure than desired. For optimal noise matching the condition is that $Z_s = Z_{opt}$, where Z_{opt} is the input impedance that minimizes the noise figure of the particular FET.

(c) *Addressing issues associated with very high Q coils*

Having previously stated that the aim of RF coil design is to reduce the coil resistance to its minimum value, one also has to consider that this may result in a very small bandwidth, the effects of which have to be considered with respect both to pulse transmission in terms of the excitation bandwidth of the RF pulses and also signal reception where the receive bandwidth may be greater than that of the RF coil.

As an example of issues in transmission mode, for 3D sequences a pulse width of 100 μs will excite an ~ 10 kHz bandwidth (note that this traditional MR definition is somewhat misleading since the bandwidth refers to the full-width-half-maximum of the approximately sinc-shaped excitation profile, meaning that in practise the tip angle at the maximum offset will have only half its value on resonance), and this means that the linewidth due to B_0 inhomogeneities must be below this value for the entire sample to be uniformly excited. However, for multi-slice excitations the excitation bandwidth of the pulse would be 1.28 kHz for a 3 mm slice thickness using a slice select gradient of 10 mT/m. For a slice 10 cm from the centre of the sample, the offset frequency would be just over 4 kHz. In this case it might be worth to add in an extra resistor during transmission to increase the coil bandwidth such that the tip angle is uniform over all slices. Another reason to reduce the Q value in transmit mode is to damp down the coil ringing after the RF pulse. The ring-down can be characterized by an exponential decay with a time constant, τ, given by:

$$\tau = \frac{2Q}{\omega} \tag{12}$$

Many authors have provided solutions to reduce the ring-down time by damping the RF coil at the end of the pulse [78–85], usually by switching in a resistive load or using a modified RF pulse with a negative lobe at the end. Currently most POC systems do not have active Q-damping, according to the descriptions in the literature, since the effects are relatively benign, resulting in a slightly smaller excitation bandwidth than from the ideal pulse shape, with fewer side-lobes. Figure 7 shows pulse ring-down associated with the three different RF coils shown in Fig. 3.

In receive mode a high Q coil can produce banding in the image, as shown in Fig. 8a. There are three well-described ways to deal with the fact that the coil bandwidth may be less, or on the order of, the acquisition bandwidth. One is to "correct" for the artifact by deconvolving by the frequency-dependent coil response function [86]. An equivalent method is to acquire a noise scan, since the noise sensitivity frequency profile reflects the receive sensitivity. A polynomial function is fitted to the noise profile, and the image is then deconvolved using this function, as shown in Fig. 8b and c, respectively.

The second method is to use inductive coupling between a secondary coil and the primary receive coil, as shown
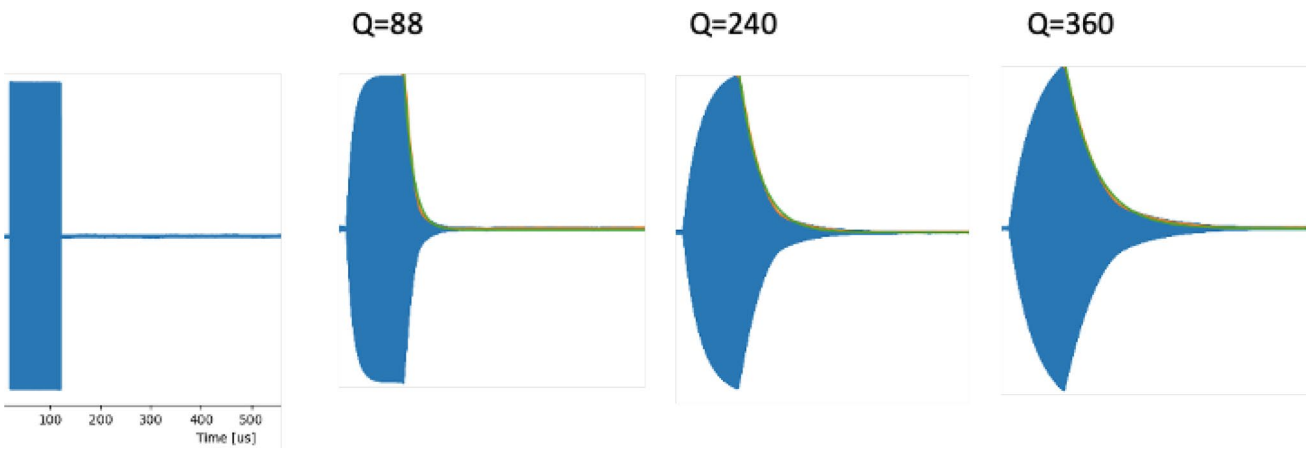
Fig. 7 Illustration of the effect of coil Q on the measured pulse shape of 100 μs duration hard RF pulse
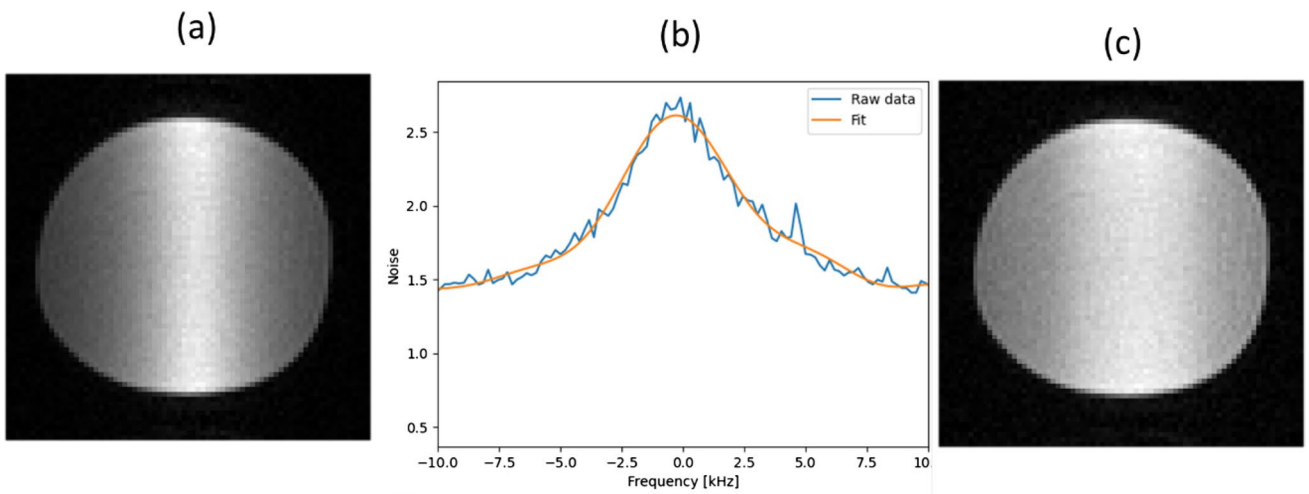

Fig. 8 Illustration of correcting the image for the frequency response of a high Q RF coil. **a** Image of a uniform phantom using an RF coil with Q value of 380. **b** Measured and fitted noise signal. **c** Deconvolution of the image with the fitted polynomial
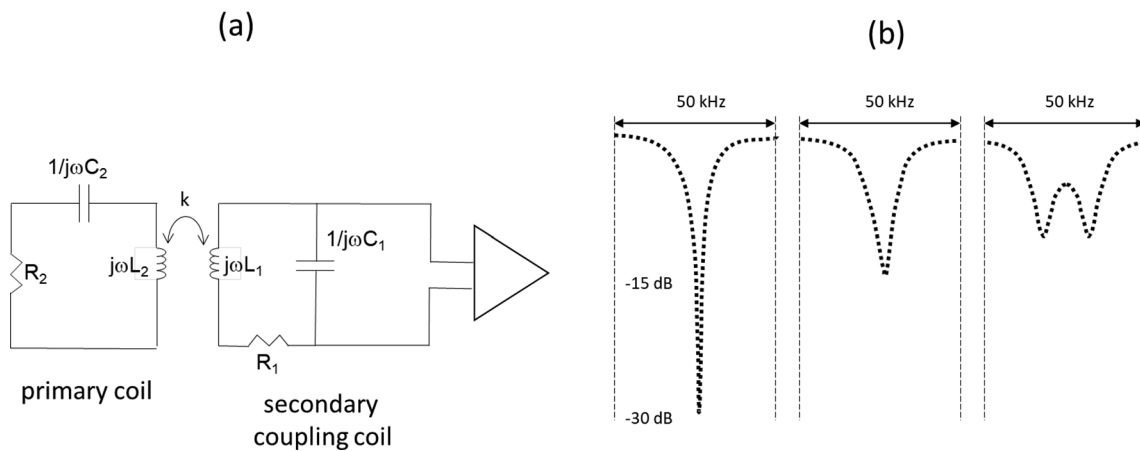

Fig. 9 **a** Increase in the effective receive bandwidth using strong coupling between a secondary coil and the primary receive coil. The effects of strong overcoupling on receive bandwidth and sensitivity. **b** Measured S_{11} parameters corresponding to, from left-to-right, weak, critical and overcoupling

in Fig. 9a: the output of the coupling coil is connected directly to a high input impedance preamplifier. Raad and Darrasse showed at 0.1 T [87] that this increased the bandwidth by a factor-of-five with an SNR reduction of less than 1 dB. To significantly increase the bandwidth of the preamplifier, the coupling must be strong (overcoupled), with ideally the Q value of the secondary coil being much larger than that of the primary coil. Under these conditions, the 1 dB bandwidth is given by:

$$B_{1dB} = 0.46\omega_p k \sqrt{\frac{Q_s}{Q_p}} \tag{13}$$

where the subscripts s and p refer to secondary and primary, respectively, and k is the coupling constant. Figure 9b shows the corresponding S-parameter plots.

The third method is to use a strong impedance mismatch between the RF coil and the preamplifier to effectively broaden the response. In this case, a preamplifier that is noise-matched rather than power-matched reduces the effective coil Q-factor without reducing the SNR [78, 79, 88–90] as shown in the analysis below.

A model of a preamplifier, shown in Fig. 10a, contains independent voltage and current noise sources, V_n and I_n, respectively. Assuming that the current and voltage noise sources in the amplifier (and all other noise sources in the circuit) are uncorrelated, then the NF is given by:

$$NF = 1 + \frac{I_n^2 |Z_{coil}|^2 + V_n^2}{4kTR_{coil}} \tag{14}$$

which importantly shows that the NF is *independen*t of the impedance across the inputs of the preamplifier. The highest SNR occurs when the RF coil and the preamplifier are noise matched as opposed to power matched. The noise matching condition is given by a purely resistive impedance:

$$R_{opt} = \frac{V_n}{I_n} \tag{15}$$

JFET transistors have optimum values ranging from 10 kΩ to 1 MΩ. A typical RF coil at low frequencies has a low resistance and is inductive (positive reactive impedance), and therefore a tuning capacitor is needed to resonate the coil, in other words to give the maximum impedance. At resonance the coil impedance is given by:

$$R_{coil} = \omega L Q \tag{16}$$

One way of increasing the effective receiver bandwidth is by incorporating a feedback loop into the preamplifier circuit, as shown in Fig. 10b, which is equivalent to adding a noiseless resistor in parallel to the input of the preamplifier, Fig. 10c, thereby changing its input impedance. The increased resistance reduces the Q of the detection circuit, thus increasing the effective bandwidth. The concept of using negative feedback in the receiver [78, 88–90] has been extensively analyzed in particular in the papers of Hoult and Kuzmin. Optimal low noise preamplifier and matching design has also been considered in the area of magnetic particle imaging [91].

The effect of the feedback capacitance on the receiver is an integrating transfer function, $H(\omega)$, given by:
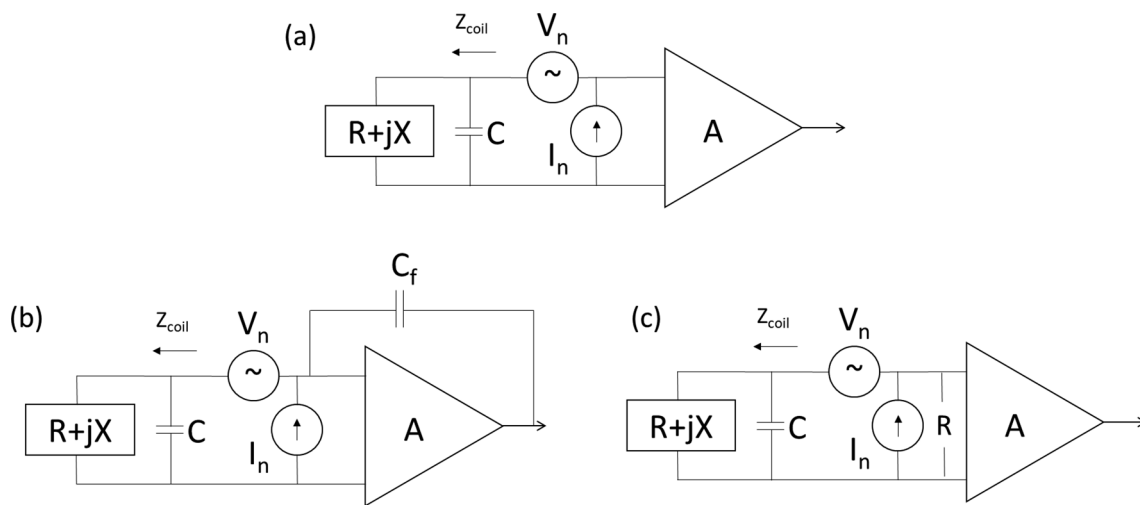

Fig. 10 **a** simplified model of an RF coil with resistance and inductive reactance, tuned with capacitor C, connected to a preamplifier with gain A, and voltage and current noise sources V_n and I_n, respectively. **b** Capacitive feedback can be used to increase the effective bandwidth of the preamplifier. **c** An equivalent circuit which has a noiseless resistor across the input of the preamplifier, therefore reducing the Q of the receiver coil without introducing extra noise

$$H(\omega) = \frac{j}{\omega\tau} \tag{17}$$

where τ is the integrating time constant. The effective input admittance is given by:

$$Y_{\text{in}} = j\omega C_{\text{f}} + \frac{C_{\text{f}}}{\tau} \tag{18}$$

Provided that $\tau > > 1/\omega$, this is equivalent to a noiseless resistor with value τ/C_{f} in parallel with the input to the preamplifier.

(d)　Data acquisition system

In line with the concepts of portability, sustainability and accessibility, most of the data acquisition systems used for POC MRI are much simpler and more compact than those associated with clinical MRI systems. This also implies that many of the features that are built into clinical systems are not present and must be added if required. Examples include eddy current compensation, gradient trimming, automatic RF power calibration, and image-based shimming. Most consoles used for POC MRI allow pulse sequence programming using relatively simple software. The key elements of a console are the timing accuracy and reproducibility of sending out both RF (magnitude and phase) and gradient pulses, accurate locking of data acquisition to RF and gradient signal transmission, the dynamic range and number of bits of the receiver, and the characteristics of the digital filters used for oversampling the data.

Examples of commercial spectrometers used for POC data acquisition include the Magritek Kea 2, the MR Solutions EVO 2, Pure Devices, Tecmag Bluestone, and RS2D Cameleon 4. Taking the Kea 2 as an example, the specifications of the system include direct digital synthesis used on the transmit side, signal reception at a fixed 100 MHz oversampled frequency, a 16-bit ADC. An inbuilt 50 Ω nominal input impedance preamplifier has a gain of 37 dB and noise figure < 1.5 dB: a passive duplexer is used as a transmit/receive switch. The Apollo Redstone has the following specifications: 10 ns minimum pulse width, 10 ns timing resolution, < 10 ns phase switching 0.0055° phase resolution, < 20 ns phase-continuous frequency switching, 64 million point waveform memory for each transmitter and gradient channel, 12.5 MHz (80 ns per complex point) digital receiver bandwidth, and up to 24-bits of digital receiver dynamic range.

Even though these consoles are significantly less expensive than their clinical counterparts, they still represent a significant fraction of the total cost of the POC system, and may also be based on proprietary software and hardware. As a result, there have been a number of different open-source MRI consoles described in the literature [92–94],

taking advantage of the rapid advances in digital technology and open-source software. In designing such systems, it is important to note that almost all of the hardware elements were originally produced for purposes other than MRI, and so it is key that features such as phase stability, inter-shot reproducibility, etc., which are very important for optimal MRI performance, are thoroughly investigated for particular designs. Michal has published a recent review of hardware which is relevant to the 10 s to 100 s kHz range [94]. Among the projects opened to the community [92–95] the Open-source Console for Real-time Acquistion (OCRA [95]) is notable for its flexibility, inexpensive off-the-shelf components, community focus, and real-time capabilities. The MAgnetic Resonance COntrol System (MaRCoS) [96] uses the same versatile hardware, however its software, firmware and FPGA firmware have been replaced to go beyond the limitations of OCRA, which included limitations on sequence length, complexity and timing precision, as well as the being written in low-level 'assembly'-style sequence programming. MaRCoS represents a complete rewrite of the server, FPGA firmware, and client software, based on a msgpack-based protocol which also supports the open-source PulSeq hardware-independent sequencing language [97]. The core of MaRCoS is the Red Pitaya SDRLab 122–16, a commercial board with two analog inputs for digitizing received data and two analog outputs for generating the RF transmit waveforms, with a bandwidth of around 50 MHz making it suitable for proton MRI at field strengths of up to 1.17 Tesla. Two receive/transmit channels are run in parallel, with frequency up/down-conversion and the bulk of the filtering handled digitally. Three digital outputs can be used for controlling RF switches or other peripherals, and one input is used for externally triggering acquisitions. The SDRLab also controls either a GPAFHDO or an OCRA1 four-channel gradient board. The MaRCoS hardware is controlled from a PC over Ethernet. On the SDRLab, sequence and acquisition data are streamed to and from an FPGA, allowing for sequences of arbitrary length. Sequences are programmed at a low level using simple arrays of times and values for each parameter, which are converted to hardware instructions by the marcos client Python library. There are several intermediate text-based interfaces to suit different styles of programming, as well as a GUI for running a range of calibrations and predefined acquisition routines.

(v)　Grounding and shielding

Two other practical issues in terms of maximizing SNR are proper grounding of all the system components and RF shielding. There are multiple active (gradient amplifiers, RF amplifier, data acquisition system) and passive (external RF shield, internal RF shield, patient table) components which represent different grounding points. With proper grounding

and filtering, connecting the RF and gradient amplifiers should ideally not add measurable noise [68]. However, it is well-known that the human body acts as an antenna for any external EMI and "guides" this EMI into the imaging region [98]. A conductive mesh cloth can be draped over the patient to reduce the body antenna effect [29, 99], but this set-up can be somewhat uncomfortable and relies on very good contact with any local shielding structures [33].

Figure 11 shows the very different noise levels that can result from different shielding and grounding conditions. In this case the system is not in a shielded room (which can reduce external sources of broadband noise by > 100 dB). The worst case occurs when the human subject is placed in the RF coil, and there is no RF shield in place, or even if the shield is in place, it is not grounded to the rest of the system. If the shield is grounded then the noise level drops by approximately a factor of 100 to a level which is almost identical to that of an unloaded coil. Similar reduction levels have been reported using conductive cloth, although authors also report that this approach is very much subject-specific [28] and the cloth typically loses performance over time.

(f) **Active cancellation of external electromagnetic interference**

Ideally, POC scanners are designed to work in challenging environments such as the ICU, emergency room, and in remote locations. Even with the system fully grounded and shielded, as described in the previous section, strong sources of electromagnetic interference (EMI) from nearby medical equipment, or general environmental EM noise, can cause artifacts which render images non-diagnostic.

Many approaches for EMI reduction in MRI/NMR have been explored in the past [100–106], with most approaches consisting of data post-processing using signals picked up from external sensors, such as additional RF coils. This type of approach has been implemented on the Hyperfine Swoop system, and was also recently shown by Srinavas et al. [33] on their 80 mT low field POC system which has multiple receive channels. A machine-learning approach for EMI cancellation has been presented by Liu et al. [34] using ten EMI-sensing coils placed close to the transmit and receive coils, underneath the patient bed, and inside the electronics cabinets. EMI interference detected by both the sensing coils and MR receive coils were used to train a five-layer convolutional neural network (CNN) model. This model was used to predict the EMI signal component in the MRI receive coil based on the signals picked up by the sensing coils: this EMI component was then subtracted from the image.

A summary of POC system characteristics from the literature

The hardware designs for a few different POC systems have been described in the literature. This section summarizes the relevant characteristics of the systems in terms of those features which directly affect the SNR.

Cooley et al. [28], operating at 80 mT (3.39 MHz) designed a Tx/Rx spiral helmet, with inner dimensions 21 cm (anterior–posterior), 17 cm (medial–lateral), matched to 50 Ω. Twelve asymmetric windings of Litz wire (AWG 20 5/39/42), with a higher turn-density near the bottom of the coil were used to optimize B_1 homogeneity: the windings extended 10.7 cm from the top of
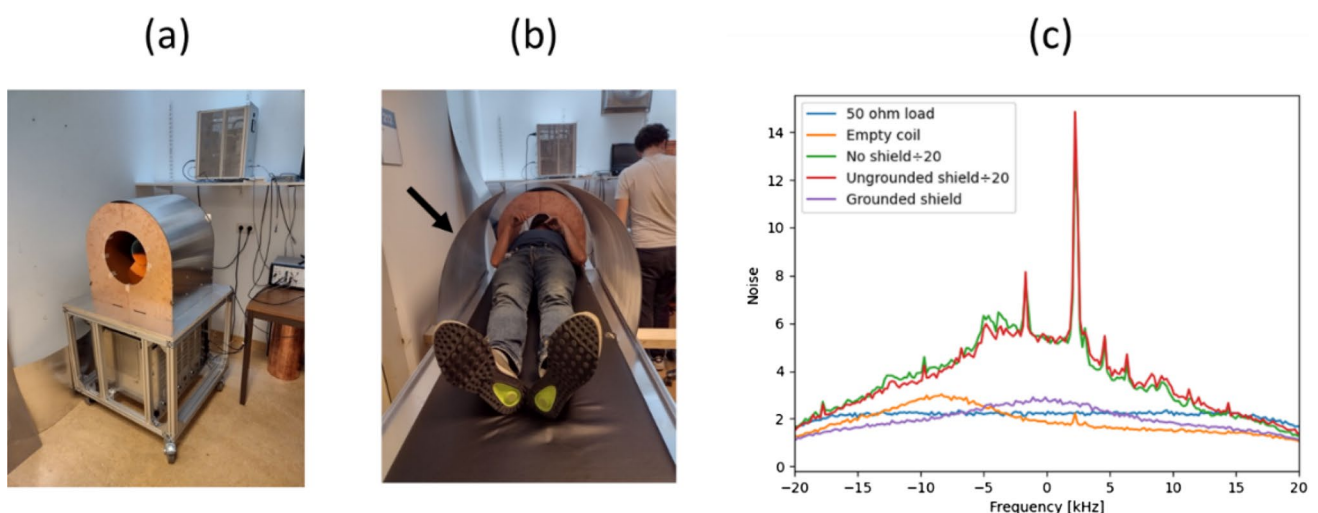

Fig. 11 a Photograph of the low-field POC system at Leiden, showing shielded magnet and grounding plate on the portable trolley. **b** Photograph of the thin semi-cylindrical aluminium RF shield which is placed around the subject being imaged. **c** Illustration of the noise levels associated with different operating and grounding conditions

the head and the coil had an inductance of 69 μH A 50 Ω input impedance, 37 dB gain pre-amplifier (MITEQ model AU-1583, Hauppauge, NY, USA) and a 24 dB second stage amplifier (Minicircuits model ZFL-500LN +, Brooklyn, NY, USA) were used. A similar geometry coil was used in work [33] at 47 mT. In this latter case a 50 Ω, 70 dB gain pre-amplifier (MITEQ P/N 1583 10 057, NY, USA) was used.

(i)   80 mT magnet with a built-in gradient of 7.6 mT/m,
(ii) loaded and unloaded Q values were 150 and 225, respectively
(iii) a hard 90° pulse of 80 μs duration required an input power of 44 W, corresponding to a transmit efficiency of 11 μT/√W.

He et al. [35], operating at 50.9 mT, used separate transmit and receive coils. The transmit coil was a variable-density elliptical solenoid of 8 turns of copper wire, three either end and one in the centre with length 24 cm and 29.4×24.8 cm diameter in the long- and short-elliptical axes. A PIN diode was used to detune the transmit coil during signal reception. The receive coil was a solenoid coil with elliptical cross-section (major axis diameter 23 cm, minor axis diameter 19 cm) constructed from enameled copper wire (2-mm diameter). An active and passive detuning module was added in the matching circuit to detune the receiver coil during RF transmission.

(i)   the receive coil had Q values of 38.7 unloaded and 37.4 loaded.

Liu et al. [34], operating at 55 mT also used separate transmit and receive coils. The receive coil was a solenoid coil with an elliptical cross-section (vertical axis 23 cm and horizontal axis 19 cm) with 10 turns and 9.5 cm length. A decoupling circuit was also implemented to detune the receive coil during RF transmission. Liu used a two-stage preamplifier module (first-stage: Gain = 30 dB; second stage: Gain = 30 dB, for input Vpp < 60 mV).

(i)   The transmit solenoid used 11 W input power for a 1 ms 180° pulse, corresponding to a transmit efficiency of 3.6 μT/√W
(ii) The Q factors of the receive coil were approximately 30 loaded and 31 unloaded.

Guallart-Naval et al. [99] designed a 70 mT Halbach array for musculoskeletal applications.

The transmit/receive coil was a standard solenoid. The receiver chain used a low-noise preamplifier with ~ 45 dB gain.

(i)   The transmit/receive coil had loaded/unloaded Q values of 88/93.

Figure 12 shows the RF coils used for neuroimaging and knee imaging in Leiden operating at 47 mT. The spiral solenoid has dimensions $235 \times 180 \times 140$ mm, 15 turns, Litz wire (1500×30 μm diameter). The knee saddle transmit coil has dimensions $185 \times 185 \times 220$ mm, 3 turns, Litz wire (1500×30 μm diameter), the knee solenoid receive coil has dimensions $155 \times 155 \times 150$ mm, 20 turns, Litz wire (1500×30 μm diameter). The network analyzer measurements show the change in S_{11} between the unloaded and loaded cases for the spiral head coil, which shows that there is a significant difference both in resonant frequency and impedance matching between the loaded and unloaded cases which must be considered.

(i)   The spiral transmit/receive coil had loaded/unloaded Q values of 215/350.
(ii) The spiral transmit/receive solenoid used 2.5 W input power for a 100 μs 90° pulse, corresponding to a transmit efficiency of 37 μT/√W.
(iii) The knee saddle transmit coil had loaded/unloaded Q values of 190/243
(iv) The knee solenoid receive coil had loaded/unloaded Q values of 240/400

Images of the brain of a healthy volunteer acquired using the Kea-2 spectrometer with a turbo spin echo sequence are shown in Fig. 13.

Discussion

There are many different POC systems that are being used for neuroimaging and musculoskeletal applications. Current POC systems have the following general characteristics in terms of the magnet and RF coil designs:

(i) B_0 field strengths between ~ 45 and ~ 80 mT
(ii) Either Tx/Rx or separate Tx and Rx RF coils, constructed either from Litz wire (unloaded Q values ~ 300–400) or copper wire (diameter ~ 2 mm, unloaded Q values ~ 30—here one should note that with larger diameter copper wire much higher unloaded Q values should be reachable). In Tx mode it is important to consider that too high a Q value would result in a transmit bandwidth which might cause tip angle and phase variations across the sample if the B_0 homogeneity is very poor, or if two-dimensional multi-slice experiments are performed,
(iii) Q-damping to reduce coil ringing in transmit mode is generally not used,

Fig. 12 Photographs of **a** the spiral Litz wire coil used for neuroimaging at 47 mT, and **b** the separate Tx (saddle) and Rx (solenoid) Litz coils used for knee imaging. **c** Plot of S_{11} with the blue line representing the impedance matched RF coil loaded with the head, and orange line the unloaded case without re-tuning. **d** Corresponding plot with the orange line now obtained after impedance matching for the unloaded case
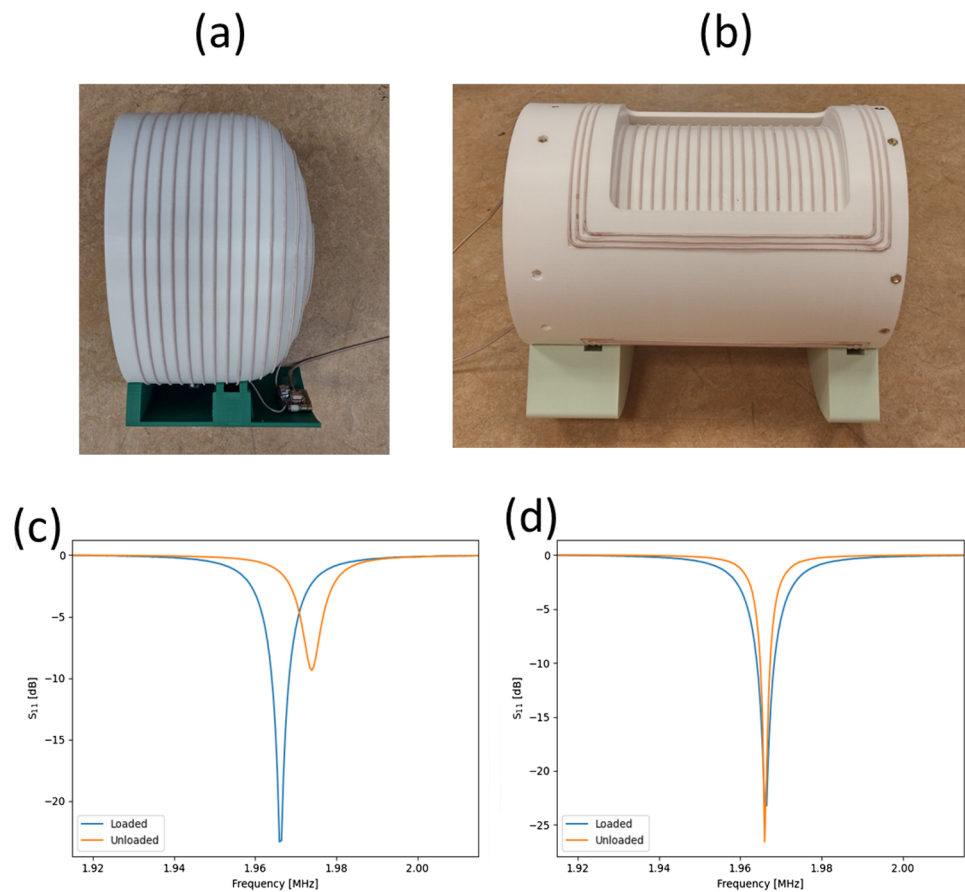
(iv)   50 Ω input impedance preamplifiers are predominantly used, accompanied by various image processing methods to reduce the effect of the limited receive bandwidth of high Q-coils (if present).

With many different types of POC low field MRI systems being developed, it is challenging to assess the performance of each different approach, especially as each element of the system (magnet, gradient coils, RF coil, gradient amplifier, RF amplifier, preamplifier and data acquisition system) may be unique to a particular configuration. One approach to performance quantitation is to design phantoms for low-field MRI, analogous to that of the American College of Radiology (ACR) for clinical field strengths, which can provide information on parameters such as SNR, geometric accuracy, high contrast spatial resolution, slice thickness accuracy, slice position accuracy, image intensity uniformity, percent signal ghosting, and low-contrast object detectability. A second approach which we are currently pursuing is to determine how close we are to the ultimate SNR, an approach which has been investigated extensively at higher fields [107, 108].

As a community, it would be very helpful to give as much information as possible on the characteristics and performance of individual elements of the POC system. With respect to the sensitivity, this includes the unloaded and loaded Q values of the transmit and receive coils, the transmit and receive sensitivities, preamplifier noise figure and gain, and specific details of the acquisition bandwidth, k-space coverage and the particular form of k-space or image domain filter. A standardized SNR mapping protocol and image reconstruction/processing pipeline could be helpful in achieving this goal. In addition to the information and parameters listed, investigators should report the details of their image reconstruction (especially the coil combination method if multi-channel Rx arrays are used, i.e., sum-of-squares vs. noise-covariance weighted optimal coil combination).
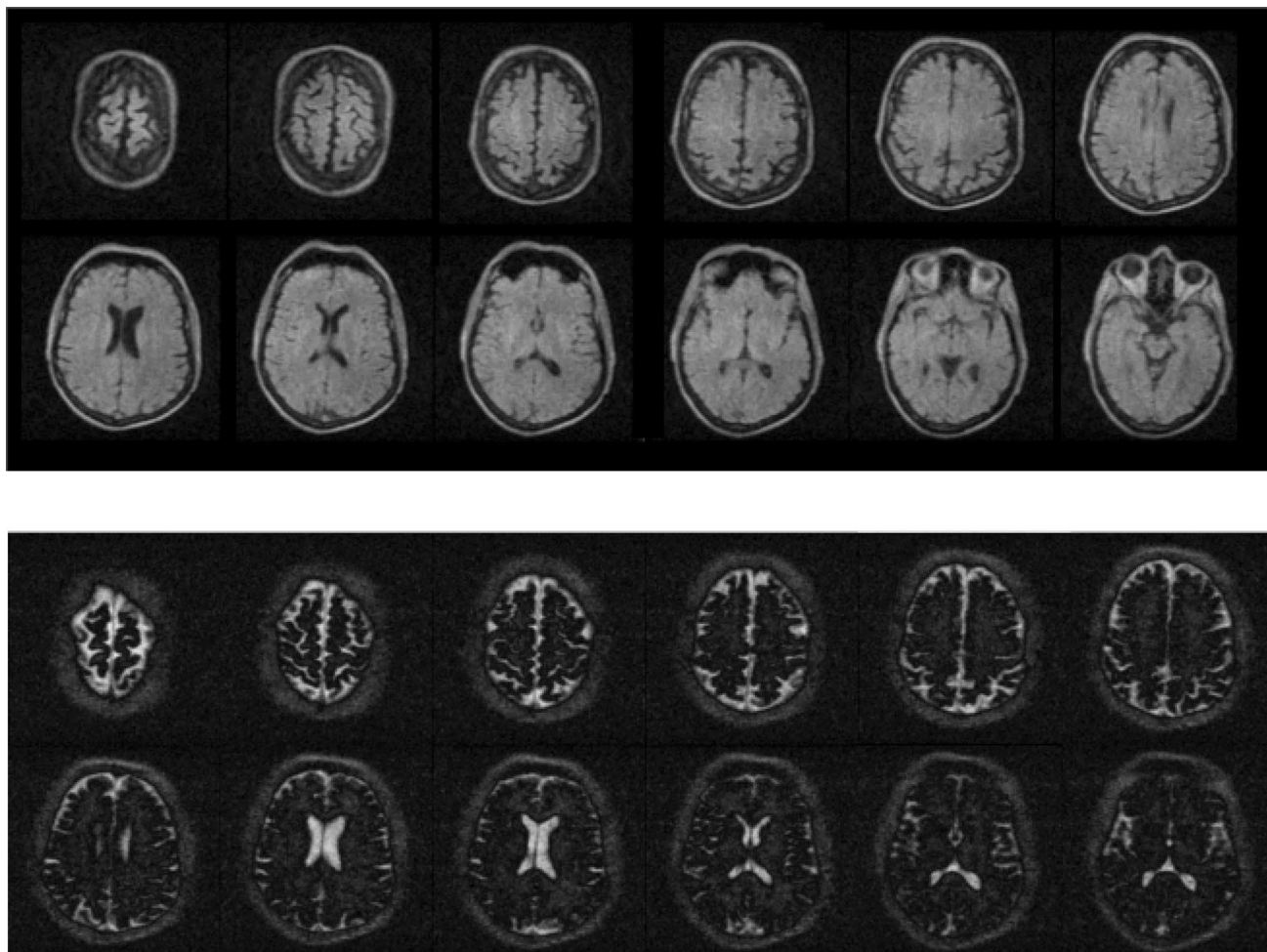
Fig. 13 In vivo images acquired at 47 mT with the high Q coil. (top) TSE sequence: field-of-view $220 \times 220 \times 225$ mm, acquisition matrix $110 \times 110 \times 75$, TR/TE 600/15 ms, echo train length 7, elliptical k-space coverage, no signal averaging, acquisition bandwidth 20 kHz, data acquisition time 9 min. (bottom) Inversion-recovery TSE: field-of-view $220 \times 220 \times 180$ mm, acquisition matrix $110 \times 110 \times 60$, TR/TI/TE 6000/200/18 ms, echo train length 110, elliptical k-space coverage, no signal averaging, acquisition bandwidth 20 kHz, data acquisition time 6.2 min

Data availability Data are available upon request from the authors.

Declarations

Conflict of interest The authors both declare no conflicts of interest.

References

1. Edelstein WA, Glover GH, Hardy CJ, Redington RW (1986) The intrinsic signal-to-noise ratio in NMR imaging. Magn Reson Med 3(4):604–618

2. Hoult DI, Lauterbur PC (1979) Sensitivity of the zeugmatographic experiment involving human samples. J Magn Reson 34(2):425–433

3. Vanheteren JG, Henkelman RM, Bronskill MJ (1987) Equivalent-circuit for coil patient interactions in magnetic-resonance-imaging. Magn Reson Imaging 5(2):93–99

4. Vanheteren JG, Henkelman RM, Bronskill MJ (1987) Application of an equivalent-circuit to signal-to-noise calculations in MRI. Magn Reson Imaging 5(2):101–108

5. Gadian DG, Robinson FNH (1979) Radiofrequency losses in NMR experiments on electrically conducting samples. J Magn Reson 34(2):449–455

6. Redpath TW, Hutchison JM (1984) Estimating patient dielectric losses in NMR imagers. Magn Reson Imaging 2(4):295–300

7. Hayden ME, Bidinosti CP, Chapple EM (2012) Specific absorption rates and signal-to-noise ratio limitations for MRI in very-low magnetic fields. Concept Magn Reson A 40A(6):281–294

8. Bandettini WP, Shanbhag SM, Mancini C, Henry JL, Lowery M, Chen MY, Xue H, Kellman P, Campbell-Washburn AE (2021) Evaluation of myocardial infarction by cardiovascular magnetic resonance at 0.55-T compared to 1.5-T. JACC Cardiovasc Imaging 14(9):1866–1868

9. Bandettini WP, Shanbhag SM, Mancini C, McGuirt DR, Kellman P, Xue H, Henry JL, Lowery M, Thein SL, Chen MCY, Campbell-Washburn AE (2020) A comparison of cine CMR imaging at 0.55 T and 1.5 T. J Cardiovasc Magn Reson. https://doi.org/10.1186/s12968-020-00618-y

10. Bhattacharya I, Ramasawmy R, Javed A, Chen MY, Benkert T, Majeed W, Lederman RJ, Moss J, Balaban RS, Campbell-Washburn AE (2021) Oxygen-enhanced functional lung imaging using a contemporary 0.55 T MRI system. NMR Biomed 34(8):e4562

11. Bhattacharya I, Ramasawmy R, Javed A, Lowery M, Henry J, Mancini C, Machado T, Jones A, Julien-Williams P, Lederman RJ, Balaban RS, Chen MY, Moss J, Campbell-Washburn AE (2022) Assessment of lung structure and regional function using 0.55 T MRI in patients with lymphangioleiomyomatosis. Invest Radiol 57(3):178–186

12. Campbell-Washburn AE, Jiang Y, Korzdorfer G, Nittka M, Griswold MA (2021) Feasibility of MR fingerprinting using a high-performance 0.55 T MRI system. Magn Reson Imaging 81:88–93

13. Campbell-Washburn AE, Malayeri AA, Jones EC, Moss J, Fennelly KP, Olivier KN, Chen MY (2021) T2-weighted lung imaging using a 0.55-T MRI system. Radiol Cardiothorac Imaging 3(3):200611

14. Campbell-Washburn AE, Mancini C, Conrey A, Edwards L, Shanbhag S, Wood J, Xue H, Kellman P, Bandettini WP, Thein SL (2022) Evaluation of hepatic iron overload using a contemporary 0.55 T MRI system. J Magn Reson Imaging 55(6):1855–1863

15. Campbell-Washburn AE, Ramasawmy R, Restivo MC, Bhattacharya I, Basar B, Herzka DA, Hansen MS, Rogers T, Bandettini WP, McGuirt DR, Mancini C, Grodzki D, Schneider R, Majeed W, Bhat H, Xue H, Moss J, Malayeri AA, Jones EC, Koretsky AP, Kellman P, Chen MY, Lederman RJ, Balaban RS (2019) Opportunities in interventional and diagnostic imaging by using high-performance low-field-strength MRI. Radiology 293(2):384–393

16. Campbell-Washburn AE, Suffredini AF, Chen MY (2021) High-performance 0.55-T lung MRI in patient with COVID-19 infection. Radiology 299(2):E246–E247

17. Kolandaivelu A, Bruce CG, Ramasawmy R, Yildirim DK, O'Brien KJ, Schenke WH, Rogers T, Campbell-Washburn AE, Lederman RJ, Herzka DA (2021) Native contrast visualization and tissue characterization of myocardial radiofrequency ablation and acetic acid chemoablation lesions at 0.55 T. J Cardiovasc Magn Reson 23(1):50

18. Qin C, Murali S, Lee E, Supramaniam V, Hausenloy DJ, Obungoloch J, Brecher J, Lin R, Ding H, Akudjedu TN, Anazodo UC, Jagannathan NR, Ntusi NAB, Simonetti OP, Campbell-Washburn AE, Niendorf T, Mammen R, Adeleke S (2022) Sustainable low-field cardiovascular magnetic resonance in changing healthcare systems. Eur Heart J Cardiovasc Imaging 23(6):e246–e260

19. Yildirim DK, Bruce C, Uzun D, Rogers T, O'Brien K, Ramasawmy R, Campbell-Washburn A, Herzka DA, Lederman RJ, Kocaturk O (2021) A 20-gauge active needle design with thin-film printed circuitry for interventional MRI at 0.55T. Magn Reson Med 86(3):1786–1801

20. Marques JP, Simonis FFJ, Webb AG (2019) Low-field MRI: an MR physics perspective. J Magn Reson Imaging 49(6):1528–1542

21. MAGNETOM Free.Max special issue RSNA Edition 2020

22. Sarracanie M, LaPierre CD, Salameh N, Waddington DEJ, Witzel T, Rosen MS (2015) Low-cost high-performance MRI. Sci Rep. https://doi.org/10.1038/srep15177

23. Tsai LL, Mair RW, Li CH, Rosen MS, Patz S, Walsworth RL (2008) Posture-dependent human He-3 lung imaging in an open-access MRI system: initial results. Acad Radiol 15(6):728–739

24. Tsai LL, Mair RW, Rosen MS, Patz S, Walsworth RL (2008) An open-access, very-low-field MRI system for posture-dependent He-3 human lung imaging. J Magn Reson 193(2):274–285

25. Koonjoo N, Shen S, Sappo C, Rosen MS (2020) Optimized quadrature head coil improves SNR in the brain at 6.5mT. Sydney, Australia

26. Straney D, Cooley CZ, Rosen MS (2020) An improved power handling active transmit/receive switch for low field MRI using reed relays. p 1395

27. Zhu B, Liu JZ, Cauley SF, Rosen BR, Rosen MS (2018) Image reconstruction by domain-transform manifold learning. Nature 555(7697):487–492

28. Cooley CZ, McDaniel PC, Stockmann JP, Srinivas SA, Cauley SF, Sliwiak M, Sappo CR, Vaughn CF, Guerin B, Rosen MS, Lev MH, Wald LL (2021) A portable scanner for magnetic resonance imaging of the brain. Nat Biomed Eng 5(3):229–239

29. O'Reilly T, Teeuwisse WM, de Gans D, Koolstra K, Webb AG (2021) In vivo 3D brain and extremity MRI at 50 mT using a permanent magnet Halbach array. Magn Reson Med 85(1):495–505

30. Yushchenko M, Sarracanie M, Salameh N (2022) Fast acquisition of propagating waves in humans with low-field MRI: toward accessible MR elastography. Sci Adv 8(36):eabo5739

31. Broche LM, Ross PJ, Davies GR, Macleod MJ, Lurie DJ (2019) A whole-body Fast Field-Cycling scanner for clinical molecular imaging studies. Sci Rep. https://doi.org/10.1038/s41598-019-46648-0

32. Nakagomi M, Kajiwara M, Matsuzaki J, Tanabe K, Hoshiai S, Okamoto Y, Terada Y (2019) Development of a small car-mounted magnetic resonance imaging system for human elbows using a 0.2 T permanent magnet. J Magn Reson 304:1–6

33. Srinivas SA, Cauley SF, Stockmann JP, Sappo CR, Vaughn CE, Wald LL, Grissom WA, Cooley CZ (2022) External dynamic interference estimation and removal (EDITER) for low field MRI. Magn Reson Med 87(2):614–628

34. Liu YL, Leong ATL, Zhao YJ, Xiao LF, Mak HKF, Tsang ACO, Lau GKK, Leung GKK, Wu EX (2021) A low-cost and shielding-free ultra-low-field brain MRI scanner. Nat Commun. https://doi.org/10.1038/s41467-021-27317-1

35. He Y, He W, Tan L, Chen F, Meng F, Feng H, Xu Z (2020) Use of 2.1 MHz MRI scanner for brain imaging and its preliminary results in stroke. J Magn Reson 319:106829

36. Huang SY, Ren ZH, Obruchkov S, Gong J, Dijkstra R, Yu W. Portable low-cost MRI system based on permanent magnets/magnet arrays. arXiv:181210474 2018

37. Ren ZH, Mu WC, Huang SY (2019) Design and optimization of a ring-pair permanent magnet array for head imaging in a low-field portable MRI system. IEEE Trans Magn 55(1):1–8

38. Podol'skii A (2002) Permanent-magnet assemblies for magnetic resonance Imaging devices for various purposes. IEEE Trans Magn 38(3):1549–1552

39. Ryu JS, Yao YY, Koh CS, Shin YJ (2006) 3-D optimal shape design of pole piece in permanent magnet MRI using parameterized nonlinear design sensitivity analysis. IEEE Trans Magn 42(4):1351–1354

40. Terada Y, Kono S, Ishizawa K, Inamura S, Uchiumi T, Tamada D, Kose K (2013) Magnetic field shimming of a permanent magnet using a combination of pieces of permanent magnets and a single-channel shim coil for skeletal age assessment of children. J Magn Reson 230:125–133

41. Prabhat AM, Crawford AL, Mazurek MH, Yuen MM, Chavva IR, Ward A Jr, Hofmann WV, Timario N, Qualls SR, Helland J, Wira C, Sze G, Rosen MS, Kimberly WT, Sheth KN (2021) Methodology for low-field, portable magnetic resonance neuroimaging at the bedside. Front Neurol. https://doi.org/10.3389/fneur.2021.760321

42. Mallinson JC (1973) One-sided fluxes—magnetic curiosity. IEEE Trans Magn 4:678–682

43. Halbach K (1980) Design of permanent multipole magnets with oriented rare-earth cobalt material. Nucl Inst Methods 169(1):1–10

44. Halbach K (1979) Strong rare-earth cobalt quadrupoles. Bull Amer Phys Soc 24(2):183–183

45. Samofalov VN, Belozorov DP, Ravlik AG (2006) Optimization of systems of permanent magnets. Phys Met Metallogr 102(5):494–505

46. Jensen JH, Abele MG (1996) Maximally efficient permanent magnet structures. J Appl Phys 79(2):1157–1163

47. Ni Mhiochain TR, Weaire D, McMurry SM, Coey JMD (1999) Analysis of torque in nested magnetic cylinders. J Appl Phys 86(11):6412–6424

48. Raich H, Blumler P (2004) Design and construction of a dipolar Halbach array with a homogeneous field from identical bar magnets: NMR Mandhalas. Concept Magn Reson B 23b(1):16–25

49. Soltner H, Blumler P (2010) Dipolar halbach magnet stacks made from identically shaped permanent magnets for magnetic resonance. Concept Magn Reson A 36a(4):211–222

50. Chen JZ, Xu CY (2007) Design and analysis of the novel test tube magnet as a device for portable nuclear magnetic resonance. IEEE Trans Magn 43(9):3555–3557

51. Kustler G (2010) Computation of NdFeB-halbach cylinders with circular and elliptical cross sections in three dimensions. IEEE Trans Magn 46(9):3601–3607

52. Turek K, Liszkowski P (2014) Magnetic field homogeneity perturbations in finite Halbach dipole magnets. J Magn Reson 238:52–62

53. Danieli E, Perlo J, Blumich B, Casanova F (2013) Highly stable and finely tuned magnetic fields generated by permanent magnet assemblies. Phys Rev Lett. https://doi.org/10.1103/PhysRevLett.110.180801

54. Blumler P, Casanova F (2015) Hardware developments: Halbach magnet arrays. Mobile NMR and MRI: developments and applications. Royal Society of Chemistry, Cambridge, pp 133–157

55. O'Reilly T, Teeuwisse W, Webb AG (2019) Three-dimensional MRI in a homogenous 27 cm diameter bore Halbach array magnet. J Magn Reson 307:106578

56. Tewari S, O'Reilly T, Webb A (2021) Improving the field homogeneity of fixed- and variable-diameter discrete Halbach magnet arrays for MRI via optimization of the angular magnetization distribution. J Magn Reson 324:106923

57. Nielsen KK, Insinga AR, Bahl CRH, Bjork R (2020) Optimizing a Halbach cylinder for field homogeneity by remanence variation. J Magn Magn Mater 514:167175

58. Purchase AR, Vidarsson L, Wachowicz K, Liszkowski P, Sun HW, Sarty GE, Sharp JC, Tomanek B (2021) A short and light, sparse dipolar halbach magnet for MRI. IEEE Access 9:95294–95303

59. Uberruck T, Blumich B (2019) Variable magnet arrays to passively shim compact permanent-yoke magnets. J Magn Reson 298:77–84

60. Lopez HS, Liu F, Weber E, Crozier S (2008) Passive shim design and a shimming approach for biplanar permanent magnetic resonance imaging magnets. IEEE Trans Magn 44(3):394–402

61. McDowell A, Conradi M (2017) Thin high-order shims for small dipole NMR magnets. J Magn Reson 281:7–16

62. Parker AJ, Zia W, Rehorn CWG, Blumich B (2016) Shimming Halbach magnets utilizing genetic algorithms to profit from material imperfections. J Magn Reson 265:83–89

63. Wenzel K, Alhamwey H, O'Reilly T, Riemann LT, Silemek B, Winter L (2021) B-0-shimming methodology for affordable and compact low-field magnetic resonance imaging magnets. Front Phys. https://doi.org/10.3389/fphy.2021.704566

64. Wang Y, Xu YJ, Wang F, Zhang JH, Peng BW, Yu P, Yu YC, Yang XD (2022) A passive shimming method for Halbach magnet based on magnetic sheet arrays. J Magn Reson 339:107210

65. Gilbert KM, Scholl TJ, Chronik BA (2008) RF coil loading measurements between 1 and 50 MHz to guide field-cycled MRI system design. Concept Magn Reson B 33b(3):177–191

66. Hoult DI, Richards RE (2011) The signal-to-noise ratio of the nuclear magnetic resonance experiment. J Magn Reson 213(2):329–343

67. Cooley CZ, Stockmann JP, Armstrong BD, Sarracanie M, Lev MH, Rosen MS, Wald LL (2015) Two-dimensional imaging in a lightweight portable MRI scanner without gradient coils. Magn Reson Med 73(2):872–883

68. de Vos B, Parsa J, Abdulrazaq Z, Teeuwisse WM, Van Speybroeck CDE, de Gans DH, Remis RF, O'Reilly T, Webb AG (2021) Design, characterisation and performance of an improved portable and sustainable low-field MRI system. Front Phys. https://doi.org/10.3389/fphy.2021.701157

69. LaPierre CD, Sarracanie M, Wald LL, Rosen MS. Parallel imaging and acceleration in the Johnson noise dominated regime. ISMRM2013. p 2772

70. Chen C-N, Hout DI (1989) Biomedical magnetic resonance technology. Adam Hilger, Bristol

71. Grafendorfer T, Conolly SM, Matter NI, Pauly JM, Scott G (2006) Optimized Litz coil design for prepolarized extremity MRI, p 2613

72. Resmer F, Seton HC, Hutchison JMS (2010) Cryogenic receive coil and low noise preamplifier for MRI at 0.01 T. J Magn Reson 203(1):57–65

73. Hoult DI (1978) The NMR receiver: a description and analysis of design. Progress NMR Spectroscopy 12:41–77

74. Mispelter J, Lupu M, Briguet A (2015) NMR probeheads for biophysical and biomedical experiments. Imperial College Press, London

75. Der E, Volotovskyy V, Sun HW, Tomanek B, Sharp JC (2018) Design of a high power PIN-diode controlled switchable RF transmit array for TRASE RF imaging. Concept Magn Reson B 48(1):e21365

76. Nacher PJ, Kumaragamage S, Tastevin G, Bidinosti CP (2020) A fast MOSFET rf switch for low-field NMR and MRI. J Magn Reson 310:106638

77. Hutchison JMS, Edelstein WA, Johnson G (1980) A whole-body NMR imaging machine. J Phys E Sci Instrum 13(9):947–955

78. Hoult DI (1979) Fast recovery, high sensitivity NMR probe and pre-amplifier for low-frequencies. Rev Sci Instrum 50(2):193–200

79. Hoult DI (1984) Fast recovery with a conventional probe. J Magn Reson 57(3):394–403

80. Conradi MS, Fet Q (1977) Switch for pulsed NMR. Rev Sci Instrum 48(3):359–361

81. Andrew ER, Jurga K (1987) NMR probe with short recovery-time. J Magn Reson 73(2):268–276

82. Jurga K, Reynhardt EC, Jurga S (1992) NMR transmit-receive system with short recovery-time and effective isolation. J Magn Reson 96(2):302–306

83. Zhen JZ, O'Neill KT, Fridjonsson EO, Stanwix PL, Johns ML (2018) A resistive Q-switch for low-field NMR systems. J Magn Reson 287:33–40

84. Peshkovsky AS, Forguez J, Cerioni L, Pusiol DJ (2005) RF probe recovery time reduction with a novel active ringing suppression circuit. J Magn Reson 177(1):67–73

85. Mandal S, Utsuzawa S, Cory DG, Hurlimann M, Poitzsch M, Song YQ (2014) An ultra-broadband low-frequency magnetic resonance system. J Magn Reson 242:113–125

86. Hrovat MI, Hersman FW, Patz S, Mair RW, Walsworth RL (2003) Signal correction for narrow bandwidth coils. p 1053

87. Raad A, Darrasse L (1992) Optimization of Nmr receiver bandwidth by inductive coupling. Magn Reson Imaging 10(1):55–65

88. Broekaert P, Jeener J (1995) Suppression of radiation damping in NMR in liquids by active electronic feedback. J Magn Reson Ser A 113(1):60–64

89. Scott G, Conolly SM, Macovski A (1996) Low field preamp matching design for high Q receiver coils. p 396

90. Kuzmin VV, Nacher PJ (2020) Signal feedback applications in low-field NMR and MRI. J Magn Reson 310:106622

91. Zheng B, Goodwill PW, Dixit N, Xiao D, Zhang WC, Gunel B, Lu KA, Scott GC, Conolly SM (2017) Optimal broadband noise matching to inductive sensors: application to magnetic particle imaging. IEEE Trans Biomed Circ Syst 11(5):1041–1052

92. Hasselwander CJ, Cao ZP, Grissom WA (2016) gr-MRI: A software package for magnetic resonance imaging using software defined radios. J Magn Reson 270:47–55

93. Michal CA (2018) A low-cost multi-channel software-defined radio-based NMR spectrometer and ultra-affordable digital pulse programmer. Concept Magn Reson B 48b(3):e21401

94. Michal CA (2020) Low-cost low-field NMR and MRI: instrumentation and applications. J Magn Reson 319:106800

95. Wald LL, McDaniel PC, Witzel T, Stockmann JP, Cooley CZ (2019) Low-cost and portable MRI. J Magn Reson Imaging. https://doi.org/10.1002/jmri.26942

96. Guallart-Naval T, O'Reilly T, Algarin JM, Pellicer-Guridi R, Vives-Gilabert Y, Craven-Brightman L, Negnevitsky V, Menkuc B, Galve F, Stockmann JP, Webb A, Alonso J (2022) Benchmarking the performance of a low-cost magnetic resonance control system at multiple sites in the open MaRCoS community. NMR Biomed 36:e4825

97. Layton KJ, Kroboth S, Jia F, Littin S, Yu H, Leupold J, Nielsen JF, Stocker T, Zaitsev M (2017) Pulseq: a rapid and hardware-independent pulse sequence prototyping framework. Magn Reson Med 77(4):1544–1552

98. Li JZ, Nie ZD, Liu YH, Wang L, Hao Y (2017) Evaluation of propagation characteristics using the human body as an antenna. Sensors 17(12):2878

99. Guallart-Naval T, Algarin JM, Pellicer-Guridi R, Galve F, Vives-Gilabert Y, Bosch R, Pallas E, Gonzalez JM, Rigla JP, Martinez P, Lloris FJ, Borreguero J, Marcos-Perucho A, Negnevitsky V, Marti-Bonmati L, Rios A, Benlloch JM, Alonso J (2022) Portable magnetic resonance imaging of patients indoors, outdoors and at home. Sci Rep. https://doi.org/10.1038/s41598-022-17472-w

100. Walsh DO (2008) Multi-channel surface NMR instrumentation and software for 1D/2D groundwater investigations. J Appl Geophys 66(3–4):140–150

101. Muller-Petke M (2020) Non-remote reference noise cancellation—using reference data in the presence of surface-NMR signals. J Appl Geophys 177:104040

102. Trushkin DV, Shushakov OA, Legchenko AV (1994) The potential of a noise-reducing antenna for surface NMR groundwater surveys in the earths magnetic-field. Geophys Prospect 42(8):855–862

103. Dalgaard E, Auken E, Larsen JJ (2012) Adaptive noise cancelling of multichannel magnetic resonance sounding signals. Geophys J Int 191(1):88–100

104. Dalgaard E, Christiansen P, Larsen JJ, Auken E (2014) A temporal and spatial analysis of anthropogenic noise sources affecting SNMR. J Appl Geophys 110:34–42

105. Larsen JJ, Dalgaard E, Auken E (2014) Noise cancelling of MRS signals combining model-based removal of powerline harmonics and multichannel Wiener filtering. Geophys J Int 196(2):828–836

106. Rearick T, Charvat GL, Rosen MS, Rothberg J (2019) Noise suppression methods and apparatus. USA

107. Ocali O, Atalar E (1998) Ultimate intrinsic signal-to-noise ratio in MRI. Magn Reson Med 39(3):462–473

108. Lattanzi R, Grant AK, Polimeni JR, Ohliger MA, Wiggins GC, Wald LL, Sodickson DK (2010) Performance evaluation of a 32-element head array with respect to the ultimate intrinsic SNR. NMR Biomed 23(2):142–151